Tuning grain boundary cation segregation with oxygen deficiency and atomic structure in a perovskite compositionally complex oxide thin film

Huiming Guo[1], Hasti Vahidi[1], Hyojoo Kang[1,2], Soham Shah[3], Mingjie Xu[4], Toshihiro Aoki[4], Timothy J. Rupert[1], Jian Luo[5], Kandis Leslie Gilliard-AbdulAziz[3,6], William J. Bowman[1,4,*]

Affiliation(s)

1. Department of Materials Science and Engineering, University of California Irvine, Irvine, CA 92697, United States.

2. Department of Materials Science and Engineering, Yonsei University, Seoul, 03722, South Korea.

3. Department of Chemical and Environmental Engineering, University of California Riverside, Riverside, CA 92521, United States.

4. Irvine Materials Research Institute (IMRI), University of California Irvine, Irvine, CA 92697, United States.

5. Department of NanoEngineering, University of California San Diego, La Jolla, CA 92093, United States.

6. Department of Civil and Environmental Engineering, University of Southern California, Los Angeles, CA 90089, United States.

*Corresponding author email: will.bowman@uci.edu

Abstract

Compositionally complex oxides (CCOs) are an emerging class of materials encompassing high entropy and entropy stabilized oxides (HEOs, ESOs). These promising advanced materials leverage tunable chemical bond structure, lattice distortion, and chemical disorder for unprecedented properties. Grain boundary (GB) and point defect segregation to GBs is relatively understudied in CCOs even though they can govern macroscopic material properties. For example, GB segregation can govern local chemical (dis)order and point defect distribution, playing a critical role in electrochemical reaction kinetics, and charge and mass transport in solid electrolytes. However, compared with conventional oxides, GBs in multi-cation CCO systems are expected to exhibit more complex segregation phenomena and thus prove more difficult to tune through GB design strategies. Here, GB segregation was studied in a model perovskite CCO $LaFe_{0.7}Ni_{0.1}Co_{0.1}Cu_{0.05}Pd_{0.05}O_{3-x}$ textured thin film by (sub-)atomic-resolution scanning transmission electron microscopy imaging and spectroscopy. It is found that GB segregation is correlated with cation reducibility—predicted by an Ellingham diagram—as Pd and Cu segregate to GBs rich in oxygen vacancies ($V_O^{\cdot\cdot}$). Furthermore, Pd and Cu segregation is highly sensitive to the concentration and spatial distribution of $V_O^{\cdot\cdot}$ along the GB plane, as well as fluctuations in atomic structure and elastic strain induced by GB local disorder, such as dislocations. This work offers a perspective of controlling segregation concentration of CCO cations to GBs by tuning reducibility of CCO cations and oxygen deficiency, which is expected to guide GB design in CCOs.

Introduction

Compositionally complex oxides (CCOs) are a new class of materials where multiple metals reside on the cation sublattice[1-3]. CCOs include high entropy oxides (HEOs) and entropy stabilized oxides (ESOs), depending on how much the role of configurational entropy influences phase stability[2,4]. High entropy oxides can form unique combinations of long-range crystallinity and local compositional disorder in the lattice[2,5]. In oxides with oxygen-metal bonds, factors such as the metal cation coordination number, bond length, angle, energy, degree of covalency, and vibration frequency are influenced by compositional complexity imposed through the distribution of metal cations, allowing tunability of functional properties, such as thermoelectric, dielectric, magnetic, electronic, ionic, thermal conductivity, and catalytic activity that are useful in energy storage and conversion[6-15].

Among various crystal structures, perovskites are fascinating candidates for high entropy design due to the existence of multiple cation sublattices, allowing a higher level of local compositional complexity[16-18]. For example, perovskite structures can have both ordered and disordered cation sublattices, while anion sublattices remain ordered[19-22]. The number of acceptor- or donor-type A or B cations in ABO_3 directly impacts charge carrier type and concentration, thereby charge transport[23]. Furthermore, the instability of perovskites under adverse conditions such as high temperature or high humidity can be enhanced by the addition of a range of cations with different activity levels in the lattice[9,24,25].

For electroceramics, in addition to chemical composition and crystal structure, defects, especially grain boundaries (GB), play an important role in their properties, e.g., they commonly serve as the rate-determined step for electrochemical processes[26-30]. Ionic conduction in all-solid-state lithium-ion battery electrolytes and solid oxide fuel/electrolysis cells are severely restricted by the sluggish charge transport across GBs—caused by the relatively high conductivity activation energy barrier, low charge mobility, or low charge carrier concentration in space charge layers at/near GBs[31-35]. Point defect segregation governs GB composition, chemical width, chemical order/disorder, electrostatic potential, and charge carrier distribution which govern GB electrochemical properties[31,36-39].

Across material classes, segregation of solutes to GBs tends to reduce the total Gibbs free energy of the system, in which case this segregation is an equilibrium phenomenon[40-45]. Equilibrium segregation is based on the intrinsic chemical properties of the system, while non-equilibrium segregation stems from systems' processing and thermal history; for example, elastic or electrostatic attraction between solutes and oxygen vacancies ($V_O^{\cdot\cdot}$) at the GB. Equilibrium segregation is typically driven by factors including the electrostatic potential at the grain boundary space charge layer. Elastic strain energy due to the lattice disorder (variation in size of solute and host atoms/ions) is another driving force, which creates lower energy GB sites for segregating solutes. One major segregation driving force is the difference in surface/bond energies, making CuO likely to segregate due to low surface/bond energies. Additionally, as demonstrated by this work, the cation reducibility is a governing factor.

Compared with conventional oxides containing a single solute/dopant cation, multi-cation CCO systems are expected to have more complex GB structure[39,45-47]. It is still not clear how GB segregation in CCOs is affected by local composition and atomic structures, such as $V_O^{\cdot\cdot}$ concentration and local strain. Elucidating cation segregation phenomena in CCOs is important for further improving properties of CCOs through GB engineering, whereby macroscopic properties can be tuned by controlling GB composition resulting from synthesis and processing.

Transition metal elements commonly serve as constituents of CCOs. For example, in electrochemical applications like electrocatalysis of the oxygen evolution reaction and electrodes of lithium-ion batteries, due to their partially occupied d-orbitals and tunable local coordination environment[48-50]. Oxide GBs can be either oxygen deficient or oxygen rich[51], but are usually viewed as a reservoir of $V_O^{\cdot\cdot}$, where their defect formation energy is much lower than in the adjacent grains[52,53]. Control of $V_O^{\cdot\cdot}$ concentration is also common during oxide synthesis, as we demonstrated recently by leveraging defect-interaction-driven exsolution of cations with high reducibility (in accordance with the Ellingham model) during exsolution-self-assembly of Pd nanorod and Pd-$Ni_xCo_{1-x}O$ core-shell nanoparticles during pulsed laser deposition (PLD) of CCO thin films[54]. Exsolution is a phase precipitation reaction that relies on cation reducibility and segregation, which in turn depends on the local $V_O^{\cdot\cdot}$ concentration enrichment that drives cation coalescence and phase precipitation[52,55]. It is also possible to leverage cation reducibility of ESOs to tune electronic

conductivity, as we showed recently by modulating electronic conductivity by 10,000 times by reversibly precipitating Cu- and Cu-rich secondary phases from the rocksalt ESO (Cu,Ni,Co,Mg,Zn)O[47].

Here, we thus hypothesize that the local reducing environment of GBs created by the accumulated $V_O^{\cdot\cdot}$ associated with electrons released from oxygen Schottky defects facilitates cation GB segregation in CCOs. It is hypothesized that the cation segregation sequence is highly sensitive to relative cation reducibility, as predicted by the Ellingham diagram, meaning that cations with higher reducibility possess greater co-segregation tendency with $V_O^{\cdot\cdot}$ driven by electrostatic point defect interactions. Additionally, the local spatial distribution of segregated cations is hypothesized to be governed by the local concentration and spatial distribution of $V_O^{\cdot\cdot}$ at GBs, which are related to non-uniform GB atomic structures and local disorders that govern the $V_O^{\cdot\cdot}$ formation energy along the GB plane. To test our hypotheses, a GB segregation study was done on a model textured perovskite CCO thin film of $LaFe_{0.7}Ni_{0.1}Co_{0.1}Cu_{0.05}Pd_{0.05}O_{3-x}$ with 5 transition-metal constituents at the B site (**Figure S1**) to decipher the role of cation reducibility, concentration, and $V_O^{\cdot\cdot}$ distribution on GB segregation.

Methods

Thin film techniques are widely employed in model studies of interfaces, stress/strain, and structure-property relations because non-equilibrium syntheses offer precise growth control of each atomic layer to make materials with specific structures of interest which are difficult or impossible to obtain using conventional bulk syntheses[48,56-61]. Aberration-corrected scanning transmission electron microscopy (STEM) imaging and spectroscopy, such as energy dispersive X-ray spectroscopy (EDS) and electron energy-loss spectroscopy (EELS), is capable of probing (sub-)nanoscale structural/chemical (dis)order[26,62,63]. Precise STEM characterization of GB chemistry requires observed GBs be at edge-on position where the GB plane is parallel to the electron beam and there is no overlap between GB and grains in the projected STEM images[27,40]. And visible atom arrangements on both sides of a GB facilitate accurate visualization of GB atomic structures. Yet, random misorientation and inclination of GBs in conventionally processed bulk polycrystalline pellets make it difficult to determine GB structure and chemistry. Compared with the bulk pellets, textured thin films offer abundant ideally oriented GBs for STEM characterization

as columnar grains grow nearly parallel to the substrate normal orientation and share a common epitaxial relationship with the substrate. In this work, we fabricate a textured $LaFe_{0.7}Ni_{0.1}Co_{0.1}Cu_{0.05}Pd_{0.05}O_{3-x}$ (CCO) thin film with $(121)_{orthorhombic}|(110)_{pseudocubic\ (pc)}$ preferred orientation by depositing the perovskite CCO on a fluorite YSZ buffer layer using (PLD, **Figure 1(a-c)**)[64]. GBs of the textured thin film can be observed under STEM by fabricating a plan-view specimen (**Figure 1(b)**). GBs form between columnar nanograins and most of them are nearly parallel to the optic axis (i.e., edge-on orientation) in the STEM high-angle annular dark-field (HAADF) images (**Figure 1(d)** and **S2(a-b)**), indicating most GB planes are parallel to electron beam. The similar $(110)_{pc}$ orientation of columnar nanograins facilitates observation of atomic arrangement at each side of GBs (**Figure 1(e)** and **S2(c)**).

The PLD used a Nd:YAG solid laser with wavelength of 266 nm and 10 ns pulse duration (Continuum SL III-10) in a high-vacuum deposition system (Neocera Pioneer 180 GLAD PLD System). Si (100) with native SiO_2 layer was used as a substrate, which was cleaned ultrasonically in acetone, isopropanol, and methanol for 5 min, respectively. Turbopump frequency and mass flow of high-purity O_2 (99.994%) are used to control oxygen partial pressure (P_{O2}). To grow the textured thin film, 4000-pulse YSZ was deposited on the Si (100) substrate surface under P_{O2} of 0.015 mTorr as a buffer layer, and then 70000-pulse CCO was deposited on the YSZ buffer layer with P_{O2} of 0.6 mtorr. The deposition temperature for both layers was set to 650 °C. The energy fluence of the laser was set as 5.3 J/cm^2 and laser rate was 5 Hz. The deposited textured CCO thin film was cooled down with 10 °C/min under P_{O2} of 0.6 mtorr. The fabrication of YSZ and CCO PLD targets is shown in **Note S1**.

The plan-view transmission electron microscope (TEM) specimen was fabricated by focus ion beam (FIB) milling in a Tescan GAIA-3 GMH FIB-scanning electron microscope (SEM). The plan-view lamella was cut at 30 kV, followed by thinning at 15 kV when the lamella thickness is below 1 µm. The Ga-ion damaged surface layers on the plan-view lamella were milled and cleaned by low-energy Ar ion beam milling at 700 eV for 30 min at each side of the lamella (Fischione Nanomill). The STEM combined with energy spectroscopy characterization was conducted in a JEOL Grand ARM300CF S/TEM with acceleration voltage of 300 kV. Chemical composition of the textured CCO thin film was investigated by STEM EDS with Dual 100 mm^2 silicon drift

detectors (SDD) under 115 pA beam current. Electronic structure of oxygen was identified by STEM EELS acquired by a Gatan GIF Quantum K2 camera with a collection semi-angle of 35.7 mrad, an EELS aperture of 2.5 mm, and a beam current of 115 pA. The crystal structure of the textured CCO thin film was identified by X-ray diffraction (XRD, **Note S2**).

Results and Discussion

It is found that Pd and Cu segregate at most GBs of the CCO from low-magnification STEM EDS mapping (**Figure 2(a-f)** and **S3(a-b)**). To quantify GB chemistry, high-magnification STEM EDS mapping was done on a randomly selected GB (**Figure 2(g-l)** and **S3(c-d)**). For the B-site cations at the GB, Pd and Cu show strong EDS signal (**Figure 2(k-l)**), Ni shows only a subtle change from the bulk behavior (**Figure S3(c)**), Co is weakly deficient (**Figure S3(d)**), while Fe is strongly deficient (**Figure 2(i)**). A-site cation La and anion O are also deficient at the GB (**Figure 2(h, j)**). The segregation width of Cu and Pd is around 1 nm from the composite EDS mapping (**Figure 2(m)**), wider than the GB core structural width of 0.35 nm visible by HAADF (**Figure 2(g)**).

Semi-quantitative EDS analysis was used to assess segregation and deficiency of each element at the CCO GB compared with the bulk grain—with assumed stoichiometry of $LaFe_{0.7}Ni_{0.1}Co_{0.1}Cu_{0.05}Pd_{0.05}O_{3-x}$. A simplified Cliff Lorimer K-factor method[40,65,66] was used for concentration calculation, Equation 1, where the concentration ratio of two elements ($\frac{C_B}{C_A}$) is proportional to their corresponding EDS signal intensity ratio ($\frac{I_B}{I_A}$) scaled by a factor k_{AB}. The EDS signal intensity profile of each element (**Figure S4**) was extracted along the direction orthogonal to the GB plane, marked as an arrow in **Figure 2(h),** and integrated over the entire EDS map area. Since EDS signals of Ni show subtle change across the GB (**Figure S3(c)** and **S4**), it is assumed that Ni occupies 10% of the B-site at the GBs and in the grains (i.e., C_{Ni} = 0.1). Concentration profiles of each other element across the GB can be acquired by calculating its K-factor with Ni (k_{X-Ni}) at both side of grains (**Table S1**), and then obtaining its concentration ratio profile with Ni ($\frac{C_X}{C_{Ni}}$) using Equation 1. The detailed calculation process is shown in **Note S3**.

$$\frac{C_B}{C_A} = k_{AB} \cdot \frac{I_B}{I_A} \quad \text{(Equation 1)}$$

It is shown that the chemical composition of the GB is significantly different than the grain region, which approaches the stoichiometric ratio (**Figure 2n**). At the GB core marked as an arrow in **Figure 2n**, Pd and Cu show around 110% and 50% higher concentration than the stoichiometric ratio, respectively, while Co, La, Fe, and O show around 20%, 15%, 30% and 20% lower than the stoichiometric ratio, respectively. At the GB deficient with O, the concentration of segregated Pd is higher than that of Cu, Ni just shows subtle concentration change, while Co shows deficiency which is less than Fe. This indicates that the amount of segregation at CCO GBs is correlated with the reducibility of cations as predicted by the Ellingham diagram, where Pd as noble metal shows strongest reducibility, and Cu shows stronger reducibility than Ni, Co and Fe as transition metals. Therefore, oxygen deficiency at GBs (**Figure 2(j, n)**) may attract cations with high reducibility, like Pd and Cu, to segregate preferentially since GBs may serve as a reservoir of $V_O^{\cdot\cdot}$ because vacancy formation energies are lower than in the grains, thus forming a local reducing environment[53,67]. This observation of preferential Pd segregation relative to less reducible transition metal cations was also observed in our prior work on this CCO during exsolution-self-assembly[54].

In addition to the segregation of Pd and Cu at GBs, it is also found that there is nonuniform distribution of Pd and Cu *along* the GB plane, where Pd and Cu aggregate at specific regions of GBs (**Figure 2(o-u)** and **S3(e-f)**). This localized non-uniform segregation along the GB plane may arise from local disorder of GBs, such as dislocation cores and $V_O^{\cdot\cdot}$ accumulation. Therefore, in addition to the chemical reducibility that governs the tendency of cation segregations, the local GB atomic structure defines the spatial distribution of cation segregation.

To prove that oxygen deficiency at GBs corresponds to the accumulation of $V_O^{\cdot\cdot}$, STEM EELS was used to track changes of electronic structure of O at GB and grains (**Figure 3(a-b)** and **S6**). The O K-edge pre-peak shows a significant decrease in intensity at the GB compared with the adjacent grains (highlighted yellow in **Figure 3(b)** and **S6**). The decrease of the O-K pre-edge intensity is regarded as appearance of $V_O^{\cdot\cdot}$ since electrons released during formation of $V_O^{\cdot\cdot}$ (Equation 2) partially fill the oxygen conduction band (or unoccupied orbitals) which will cause less electrons from core shells filling the conduction band and corresponding to weaker intensity of EELS signal at O-K

pre-edge[31,68-70]. This EEL spectra change of O-K edge at GB correspond well with oxygen deficiency shown in the STEM EELS and EDS elemental mapping (**Figure S5**), so the accumulated $V_O^{\cdot\cdot}$ at GBs induce segregation of cations with high reducibility in CCOs due to their lower co-segregation energy with $V_O^{\cdot\cdot}$[71-73].

$$O_O^{\times} \rightarrow V_O^{\cdot\cdot} + 2e' + \frac{1}{2}O_{2\,(gas)} \quad \text{(Equation 2)}$$

Additionally, it is found that different GBs show different segregation behavior. In the triple junction shown in **Figure 3(c)**, GB 1 shows much higher EDS signal of Pd and Cu and less EDS signal of O than GB 2 and GB 3 (**Figure 3(d-e)**). This indicates that more severe oxygen deficiency may cause more Pd and Cu to segregate at GBs. The oxygen deficiency may show great deviations in GBs since even subtle change of 5 degrees of freedom, which describe misorientation and GB plane direction, and additional 3 microscopic degrees of freedom, which describe local atom arrangement, will create very different GB structures and vacancy formation energies[37,74,75]. Therefore, semi-quantitative EDS analysis was done on a series of 9 GBs to decipher the variations of oxygen deficiency and its role in segregation concentration of Pd and Cu (**Figure 3(g)**). In the 9 survey GBs, oxygen deficiency at the GB core varies from 4.3% to 18.4% relative to the stoichiometric concentration. The concentration of Pd, Cu, and combined Pd and Cu at the GB core tend upwards with oxygen deficiency or $V_O^{\cdot\cdot}$ accumulation, although exceptions exist in some GBs arising from specific GB structure (**Figure 3(g)**). Therefore, CCO GBs with higher concentration of $V_O^{\cdot\cdot}$ will induce a greater number of reducible cations to segregate, which provides a perspective to engineer GBs to improve properties of CCOs becuase cation segregation concentration of CCOs can be controlled by modifying oxygen deficiency of GBs through CCO/HEO/ESO composition design, synthesis, and post-processing.

To track the role of localized strain in GB segregation, a low-angle tilt GB made up of a dislocation array was characterized with STEM EDS mapping, together with geometric phase analysis (GPA) which identifies lattice distortion around dislocation cores[76-80] (**Figure 4(a-h)**). It is found that Pd and Cu locally segregate around the dislocation cores where the oxygen is deficient (**Figure 4(a-f)**). The GPA shows that the extra-half atomic plane introduces intense compressive strain in surroundings and corresponding tensile strain at the other side of the dislocation core (**Figure 4(g-h)**). The profile of GB chemical change and strain distribution along the dislocation array, marked

as an arrow in **Figure 4(b)**, indicates that the oxygen deficiency and corresponding Pd and Cu segregation are localized at the regions with strong strain, highlighted as yellow in **Figure 4(i)**. It has been reported that either compressive or tensile strain may decrease the formation energy of $V_O^{\cdot\cdot}$ to enhance $V_O^{\cdot\cdot}$ concentration at strained regions[68,81,82]. Therefore, in this CCO system, cations with high reducibility prefer to segregate at strongly strained regions with locally accumulated $V_O^{\cdot\cdot}$.

Conclusions

To summarize, a textured thin film of a model perovskite CCO ($LaFe_{0.7}Ni_{0.1}Co_{0.1}Cu_{0.05}Pd_{0.05}O_{3-x}$) was prepared by PLD and its plan-view specimen was used to decipher the role of CCO composition and GB atomic structure in cation segregation at GBs of this multi-cation system (**Figure 5**). GB structure, chemistry and local disorder are probed by (sub)-nanoscale-resolution STEM associated with EDS, EELS, and GPA. Compared with Ni, Co, and Fe, the greater reducibility of Pd and Cu yield significant GB segregation closely correlated with oxygen deficiency, indicating cation reducibility governs the segregation concentration of the CCO GBs which can be predicted by the Ellingham diagram (**Figure 5(a)**). Additionally, oxygen deficiency in the lattice arises from formation of Schottky defects (**Figure 5(b)**), so the oxygen deficiency at GBs corresponds to accumulation of $V_O^{\cdot\cdot}$, which was confirmed by tracking changes of the O-K edge EELS pre-peak. Therefore, accumulated $V_O^{\cdot\cdot}$ and electrons they released make GBs an environment compatible with cations with greater reducibility, leading them to segregate due to their low co-segregation energy of $V_O^{\cdot\cdot}$ (**Figure 5(b-c)**). In addition to compositions of CCOs, GB nanostructures also contribute to the cation segregation concentration by modifying the extent and distribution of oxygen deficiency (**Figure 5(c)**). Generally, concentration of Pd and Cu tend upwards with oxygen deficiency or $V_O^{\cdot\cdot}$ accumulation. Strongly strained regions around dislocation cores facilitate the formation of $V_O^{\cdot\cdot}$ and thus induce localized segregation of Pd and Cu. This work introduces the novel perspective that cation segregation concentration of CCO GBs can be controlled by CCO composition through the incorporation of cations based on their Ellingham reducibility, and the extent and distribution of oxygen deficiency along the GB plane, which should broadly inform as the strategies to engineer GBs within the CCO community.

Figures

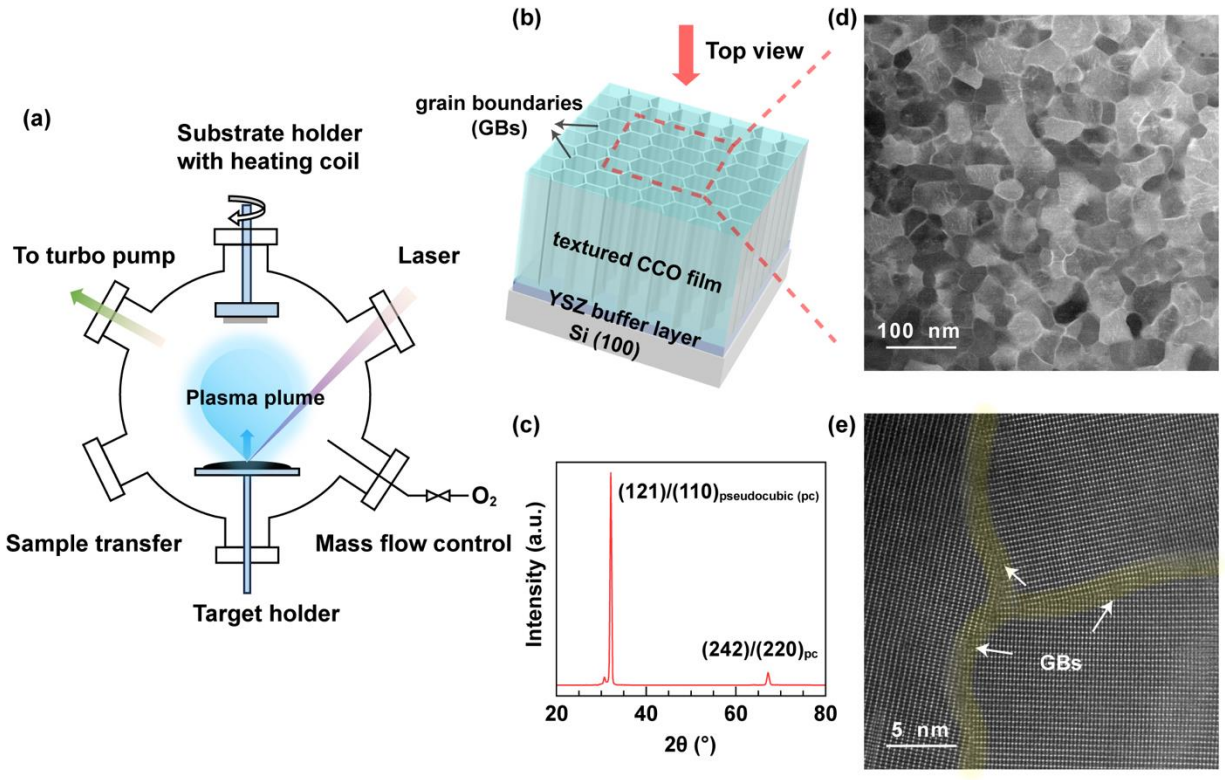

Fig. 1. Preparation and characterization of a plan-view textured perovskite CCO thin film for GB segregation study. (a) Schematic of thin film fabrication with pulsed laser deposition (PLD). (b) Schematic of the prepared textured CCO thin film grown on Si (100) with a YSZ buffer layer, where lots of grain boundaries (GBs) form between columnar grains. Plan-view TEM specimen was fabricated by FIBs for GB segregation study (marked as a red rectangle). (c) XRD pattern of the fabricated CCO thin film showing textures of $(110)_{\text{pseudocubic (pc)}}$ orientation. The satellite peak at the left of (121)/(110) is diffraction of the W X-rays from the X-ray source. (d) Low-magnified STEM HAADF image of the plan-view CCO thin film specimen, where GBs between columnar

nanograins are sharp and clear. (e) High-magnified STEM HAADF image of a triple junction where local grains possess strong $(110)_{pc}$ orientation texture.

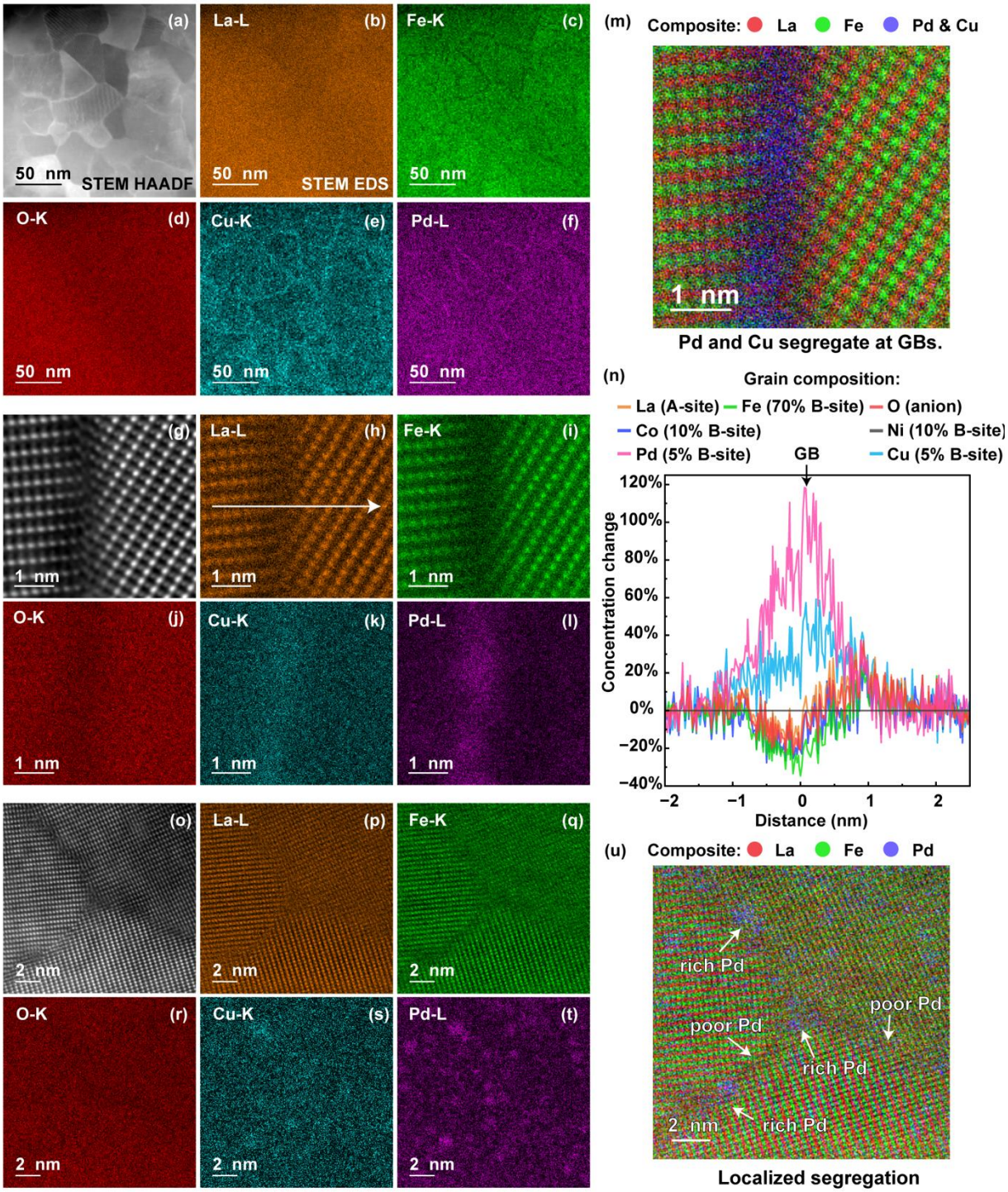

Fig. 2 Pd and Cu segregation at CCO GBs. (a-f) Low-magnification STEM EDS mapping of the plan-view specimen of the CCO textured thin film: (a) STEM HAADF survey image; (b) La-L; (c) Fe-K; (d) O-K; (e) Cu-K; and (f) Pd-L. (g-m) High-magnification STEM EDS mapping of a CCO GB: (g) STEM HAADF survey image; (h) La-L with filter; (i) Fe-K with filter; (j) O-K; (k) Cu-K; (l) Pd-K; and (m) composite of La (red), Fe (green), mixed Cu and Pd (blue). (n) Concentration changes of each element across the GB shown in (g). The concentration profile is generated via extracting the profile of EDS signal along the direction perpendicular to the GB (marked as a white arrow in (h)) and integral all the EDS signals, and then converting the EDS signal intensity to concentration with K-factor method. (o-u) STEM EDS mapping of a CCO triple junction: (o) STEM HAADF survey image; (p) La-L with filter; (q) Fe-K with filter; (r) O-K; (s) Cu-K; (t) Pd-K; and (u) composite of La (red), Fe (green) and Pd (blue). The nonuniform distribution of Cu and Pd at GBs indicates localized GB structure may dominate dopant segregation.

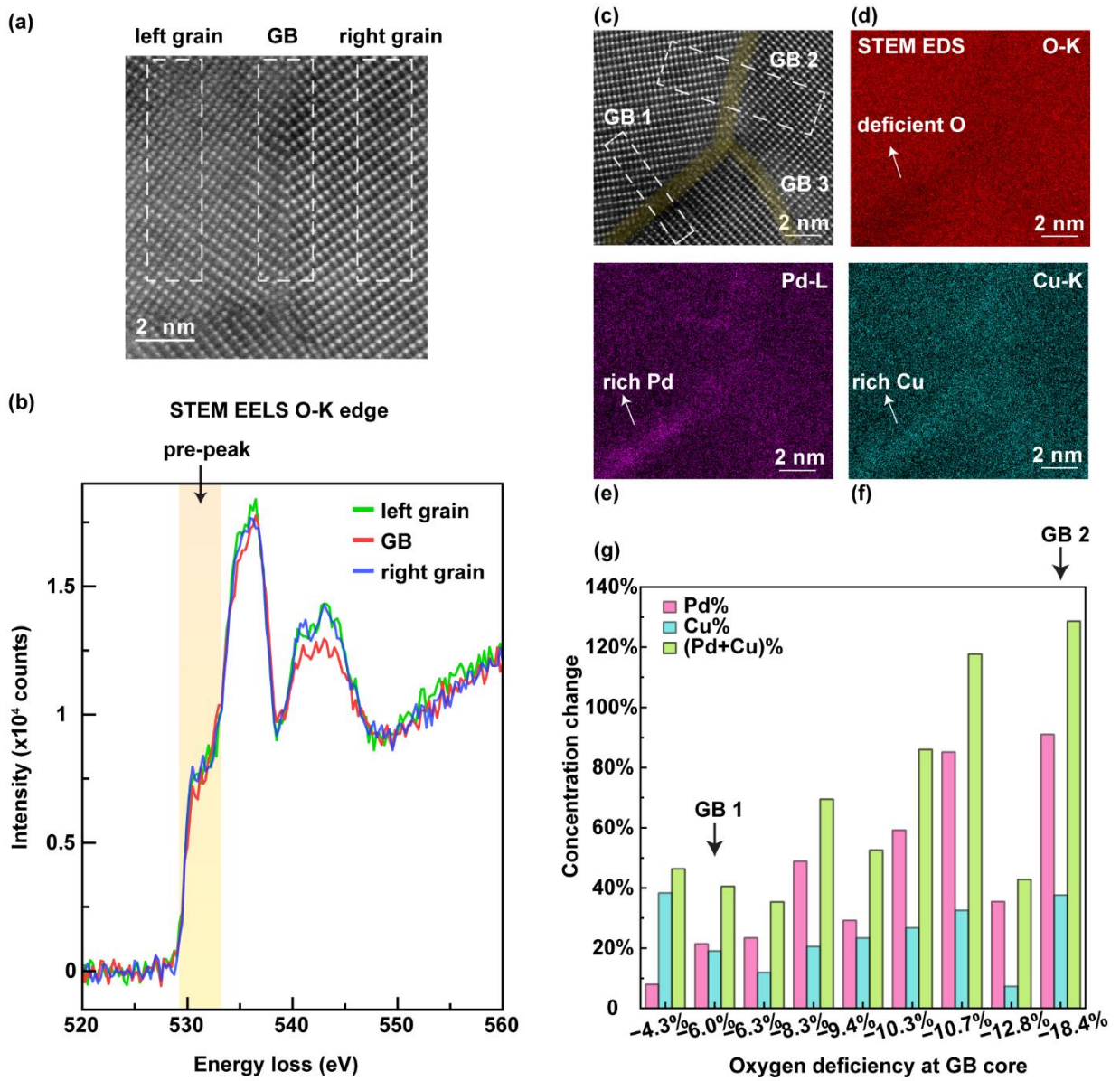

Fig. 3. Oxygen deficiency at GBs induces segregation of Pd and Cu characterized by STEM EELS and EDS. (a-b) STEM HAADF survey image of a GB in the CCO textured thin film (a), and corresponding EEL spectra of this GB, its left grain, and right grain (b), which are extracted from EELS mapping of the marked rectangle regions shown in (a). The EELS data were collected under dispersion of 0.25 eV/channel. (c-f) STEM HAADF survey image of a triple junction (c), and corresponding STEM EDS mapping of O (d), Pd (e), and Cu (f), which shows the region with more oxygen deficiency attracts more segregation of Pd and Cu. (g) Statistics on the role of oxygen deficiency in concentration change of Pd (pink), Cu (blue), and combined Cu and Pd (green) at GBs from semi-quantitative EDS analysis on a series of CCO GBs.

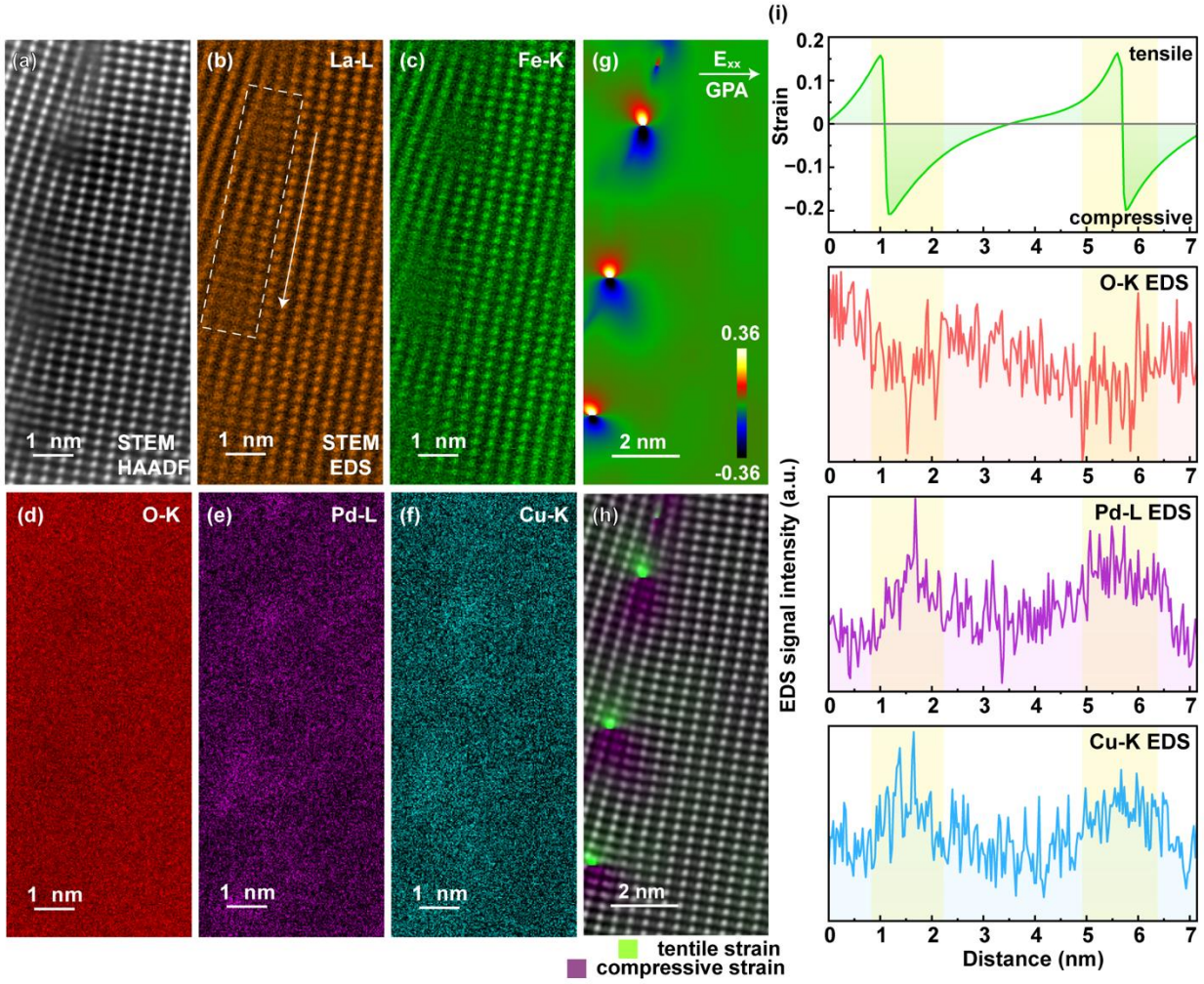

Fig. 4. Strong strain at dislocation cores induces localized oxygen deficiency and results in localized segregation of Cu and Pd. (a-f) STEM HAADF survey image of a low-angle tilt GB made up of a dislocation array (a), and corresponding STEM EDS mapping of filtered La-L (b), filtered Fe-K (c), O-K (d), Pd-L (e) and Cu-K (f). (g-h) Strain mapping around this GB along the marked E_{xx} direction via geometric phase analysis (GPA) (g), and composite image of the STEM HAADF and GPA strain mapping along E_{xx} direction (h) to locate atomic arrangement causing the tensile strain (green) and compressive strain (purple) at this GB. (i) Profile of strain and EDS signal intensity along the GB dislocation array marked as an arrow in (b), integrated with data within the white rectangle (b). The regions with strong strain show severe deficiency of oxygen and rich EDS intensity of Pd and Cu, which are highlighted as yellow.

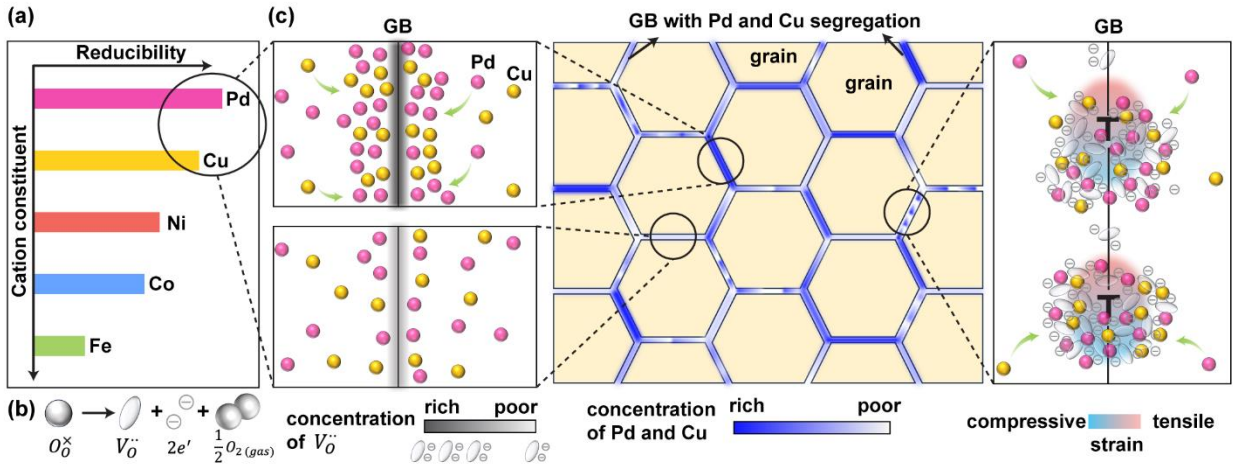

Fig. 5. Schematic illustration of the role of cation reducibility, oxygen deficiency, and localized strain in GB segregation of *the model* CCO. (a) Pd and Cu with relatively strong reducibility prefer to segregate at GBs with oxygen deficiency. (b) Oxygen deficiency is caused by Schottky defects of oxygen, where $V_O^{\cdot\cdot}$ and electrons occupy oxygen lattice sites, while oxygen anions escape to the surface. (c) Schematics of GBs of the CCO with nonuniform Pd and Cu segregation. The high and low segregated concentration may arise from severe and light oxygen deficiency at GBs, respectively. The localized segregation of Pd and Cu is contributed by localized intense strain regions that enhance formation of $V_O^{\cdot\cdot}$ via dropping their formation energy.

Supplementary information is available with this article.

Acknowledgments

HG and WJB acknowledge NSF CAREER (DMR- 2042638) and ACS PRF (61961-DNI). HV, TJR, JL, and WJB were primarily supported by the National Science Foundation Materials Research Science and Engineering Center program through the UC Irvine Center for Complex and Active Materials (DMR-2011967). SS and KGA were primarily supported through the Center for Complex and Active Materials seed program. The authors acknowledge the use of facilities and instrumentation at the UC Irvine Materials Research Institute (IMRI), which is supported in part by the National Science Foundation through the UC Irvine Materials Research Science and Engineering Center (DMR-2011967).

Author declarations section (conflict of interest, ethics approval, and author contributions)

No conflicts of interest. HG and WJB designed and conceptualized the study. SS synthesized the CCO powder under the advice of KGA. HG fabricated the CCO PLD target, grew the PLD films, prepared the STEM specimen, and worked with MX and TA on data acquisition. HG analyzed and processed the data, and interpreted the processed data with WJB . HG and HV drafted the manuscript under the advice of WJB. TJR and JL critically reviewed and provided intellectual guidance on the manuscript contents. WJB supervised the research.

Data availability statement

Data is available upon request.

References

1 Xin Wang, Justin Cortez, Alexander D. Dupuy, Julie M. Schoenung, and William J. Bowman, Materials Research Letters **11** (3), 196 (2023).

2 Matthew Brahlek, Maria Gazda, Veerle Keppens, Alessandro R. Mazza, Scott J. McCormack, Aleksandra Mielewczyk-Gryń, Brianna Musico, Katharine Page, Christina M. Rost, Susan B. Sinnott, Cormac Toher, Thomas Z. Ward, and Ayako Yamamoto, APL Materials **10** (11), 110902 (2022).

3 Andrew J. Wright and Jian Luo, Journal of Materials Science **55** (23), 9812 (2020).

4 Andrew J. Wright, Qingyang Wang, Chuying Huang, Andy Nieto, Renkun Chen, and Jian Luo, Journal of the European Ceramic Society **40** (5), 2120 (2020).

5 Solveig S. Aamlid, Mohamed Oudah, Jörg Rottler, and Alannah M. Hallas, Journal of the American Chemical Society **145** (11), 5991 (2023).

6 Ping Zhang, Zhihao Lou, Mengjie Qin, Jie Xu, Jiatong Zhu, Zongmo Shi, Qian Chen, Michael J. Reece, Haixue Yan, and Feng Gao, Journal of Materials Science & Technology **97**, 182 (2022).

7 Wei Xiong, Hangfeng Zhang, Shuyao Cao, Feng Gao, Peter Svec, Jan Dusza, Michael J. Reece, and Haixue Yan, Journal of the European Ceramic Society **41** (4), 2979 (2021).

8 Lei Su, Huaixun Huyan, Abhishek Sarkar, Wenpei Gao, Xingxu Yan, Christopher Addiego, Robert Kruk, Horst Hahn, and Xiaoqing Pan, Nature Communications **13** (1), 2358 (2022).

9 Yinchun Shi, Na Ni, Qi Ding, and Xiaofeng Zhao, Journal of Materials Chemistry A **10** (5), 2256 (2022).

10 D. Bérardan, S. Franger, A. K. Meena, and N. Dragoe, Journal of Materials Chemistry A **4** (24), 9536 (2016).

11 Liang Xu, Lei Su, Hongjie Wang, Hongfei Gao, De Lu, Kang Peng, Min Niu, and Zhixin Cai, Journal of the American Ceramic Society **105** (2), 1548 (2022).

12 Chang Deng, Tao Wang, Peiwen Wu, Wenshuai Zhu, and Sheng Dai, Nano Energy **120**, 109153 (2024).

13 Abhishek Sarkar, Leonardo Velasco, Di Wang, Qingsong Wang, Gopichand Talasila, Lea de Biasi, Christian Kübel, Torsten Brezesinski, Subramshu S. Bhattacharya, Horst Hahn, and Ben Breitung, Nature Communications **9** (1), 3400 (2018).

14 Rui Zhang, Chunyang Wang, Peichao Zou, Ruoqian Lin, Lu Ma, Liang Yin, Tianyi Li, Wenqian Xu, Hao Jia, Qiuyan Li, Sami Sainio, Kim Kisslinger, Stephen E. Trask, Steven N. Ehrlich, Yang Yang, Andrew M. Kiss, Mingyuan Ge, Bryant J. Polzin, Sang Jun Lee, Wu Xu, Yang Ren, and Huolin L. Xin, Nature **610** (7930), 67 (2022).

15 Yan Zeng, Bin Ouyang, Jue Liu, Young-Woon Byeon, Zijian Cai, Lincoln J. Miara, Yan Wang, and Gerbrand Ceder, Science **378** (6626), 1320 (2022).

16 Yuhao Wang, Jiapeng Liu, Yufei Song, Jing Yu, Yunfeng Tian, Matthew James Robson, Jian Wang, Zhiqi Zhang, Xidong Lin, Guodong Zhou, Zheng Wang, Longyun Shen, Hailei Zhao, Salvatore Grasso, and Francesco Ciucci, Small Methods **7** (4), 2201138 (2023).

17 Sicong Jiang, Tao Hu, Joshua Gild, Naixie Zhou, Jiuyuan Nie, Mingde Qin, Tyler Harrington, Kenneth Vecchio, and Jian Luo, Scripta Materialia **142**, 116 (2018).

[18] Dong Chen, Siyang Nie, Liang Wu, Xiao Zheng, Shengyu Du, Xiaolan Duan, Qiang Niu, Pengfei Zhang, and Sheng Dai, Chemistry of Materials **34** (4), 1746 (2022).

[19] Jason Luong, Xin Wang, Alicia Tsung, Nicholas Humphrey, Huiming Guo, Benjamin X. Lam, Shaama Mallikarjun Sharada, and William J. Bowman, ACS Applied Nano Materials **6** (3), 1620 (2023).

[20] Tao Wang, Hao Chen, Zhenzhen Yang, Jiyuan Liang, and Sheng Dai, Journal of the American Chemical Society **142** (10), 4550 (2020).

[21] Tuncay Erdil and Cigdem Toparli, ACS Applied Energy Materials **6** (21), 11255 (2023).

[22] Abhishek Sarkar, Ruzica Djenadic, Di Wang, Christina Hein, Ralf Kautenburger, Oliver Clemens, and Horst Hahn, Journal of the European Ceramic Society **38** (5), 2318 (2018).

[23] Yuhao Wang, Matthew James Robson, Alessandro Manzotti, and Francesco Ciucci, Joule **7** (5), 848 (2023).

[24] Zuoqing Liu, Zhengjie Tang, Yufei Song, Guangming Yang, Wanru Qian, Meiting Yang, Yinlong Zhu, Ran Ran, Wei Wang, Wei Zhou, and Zongping Shao, Nano-Micro Letters **14** (1), 217 (2022).

[25] Dawei Zhang, Héctor A. De Santiago, Boyuan Xu, Cijie Liu, Jamie A. Trindell, Wei Li, Jiyun Park, Mark A. Rodriguez, Eric N. Coker, Joshua D. Sugar, Anthony H. McDaniel, Stephan Lany, Liang Ma, Yi Wang, Gregory Collins, Hanchen Tian, Wenyuan Li, Yue Qi, Xingbo Liu, and Jian Luo, Chemistry of Materials **35** (5), 1901 (2023).

[26] Hasti Vahidi, Komal Syed, Huiming Guo, Xin Wang, Jenna L. Wardini, Jenny Martinez, and William J. Bowman, in *Crystals* (2021), Vol. 11.

[27] William J. Bowman, Jiangtao Zhu, Renu Sharma, and Peter A. Crozier, Solid State Ionics **272**, 9 (2015).

[28] Emily Milan and Mauro Pasta, Materials Futures **2** (1), 013501 (2023).

[29] Xiaoming Liu, Regina Garcia-Mendez, Andrew R. Lupini, Yongqiang Cheng, Zachary D. Hood, Fudong Han, Asma Sharafi, Juan Carlos Idrobo, Nancy J. Dudney, Chunsheng Wang, Cheng Ma, Jeff Sakamoto, and Miaofang Chi, Nature Materials **20** (11), 1485 (2021).

[30] Xin Xu, Yuzi Liu, Jie Wang, Dieter Isheim, Vinayak P. Dravid, Charudatta Phatak, and Sossina M. Haile, Nature Materials **19** (8), 887 (2020).

[31] William J. Bowman, Madeleine N. Kelly, Gregory S. Rohrer, Cruz A. Hernandez, and Peter A. Crozier, Nanoscale **9** (44), 17293 (2017).

[32] Arseniy Bokov, Jeffery A. Aguiar, Matthew L. Gong, Alexey Nikonov, and Ricardo H. R. Castro, The Journal of Physical Chemistry C **122** (46), 26344 (2018).

[33] Xin Guo and Rainer Waser, Progress in Materials Science **51** (2), 151 (2006).

[34] Tomasz Polczyk, Wojciech Zając, Magdalena Ziąbka, and Konrad Świerczek, Journal of Materials Science **56** (3), 2435 (2021).

[35] Tom Lee, Ji Qi, Chaitanya A. Gadre, Huaixun Huyan, Shu-Ting Ko, Yunxing Zuo, Chaojie Du, Jie Li, Toshihiro Aoki, Ruqian Wu, Jian Luo, Shyue Ping Ong, and Xiaoqing Pan, Nature Communications **14** (1), 1940 (2023).

[36] William J. Bowman, Amith Darbal, and Peter A. Crozier, ACS Applied Materials & Interfaces **12** (1), 507 (2020).

[37] Xiaorui Tong, William J. Bowman, Alejandro Mejia-Giraldo, Peter A. Crozier, and David S. Mebane, The Journal of Physical Chemistry C **124** (43), 23619 (2020).

[38] Moritz Kindelmann, Sonia Escolastico, Laura Almar, Ashok Vayyala, Dylan Jennings, Wendelin Deibert, Wilhelm A. Meulenberg, Wolfgang Rheinheimer, Martin Bram, Jose M. Serra, Joachim Mayer, and Olivier Guillon, ChemRxiv. (2023).
[39] Shu-Ting Ko, Tom Lee, Ji Qi, Dawei Zhang, Wei-Tao Peng, Xin Wang, Wei-Che Tsai, Shikai Sun, Zhaokun Wang, William J. Bowman, Shyue Ping Ong, Xiaoqing Pan, and Jian Luo, Matter **6** (7), 2395 (2023).
[40] Komal Syed, Mingjie Xu, Kenta K. Ohtaki, David Kok, Keyur K. Karandikar, Olivia A. Graeve, William J. Bowman, and Martha L. Mecartney, Materialia **14**, 100890 (2020).
[41] Komal Syed, Nadjia B. Motley, and William J. Bowman, Acta Materialia **227**, 117685 (2022).
[42] P. Wynblatt, G. S. Rohrer, and F. Papillon, Journal of the European Ceramic Society **23** (15), 2841 (2003).
[43] N. D. Browning, R. F. Klie, and Y. Lei, presented at the Mixed Ionic Electronic Conducting Perovskites for Advanced Energy Systems, Dordrecht, 2004 (unpublished).
[44] J. Nowotny, C. C. Sorrell, and T. Bak, Surface and Interface Analysis **37** (3), 316 (2005).
[45] Megan J. McCarthy, Hui Zheng, Diran Apelian, William J. Bowman, Horst Hahn, Jian Luo, Shyue Ping Ong, Xiaoqing Pan, and Timothy J. Rupert, Physical Review Materials **5** (11), 113601 (2021).
[46] Jian Luo and Naixie Zhou, Communications Materials **4** (1), 7 (2023).
[47] Hasti Vahidi, Alexander D. Dupuy, Benjamin X. Lam, Justin Cortez, Pulkit Garg, Timothy J. Rupert, Julie M. Schoenung, and W.J. Bowman, Advanced Functional Materials (In Press) (2024).
[48] Weiwei Li, Jueli Shi, Kelvin H. L. Zhang, and Judith L. MacManus-Driscoll, Materials Horizons **7** (11), 2832 (2020).
[49] Mohana V. Kante, Moritz L. Weber, Shu Ni, Iris C. G. van den Bosch, Emma van der Minne, Lisa Heymann, Lorenz J. Falling, Nicolas Gauquelin, Martina Tsvetanova, Daniel M. Cunha, Gertjan Koster, Felix Gunkel, Slavomír Nemšák, Horst Hahn, Leonardo Velasco Estrada, and Christoph Baeumer, ACS Nano **17** (6), 5329 (2023).
[50] Jihyun Baek, Md Delowar Hossain, Pinaki Mukherjee, Junghwa Lee, Kirsten T. Winther, Juyoung Leem, Yue Jiang, William C. Chueh, Michal Bajdich, and Xiaolin Zheng, Nature Communications **14** (1), 5936 (2023).
[51] Qizhang Yan, Chongze Hu, and Jian Luo, Submitted (2023).
[52] Komal Syed, Jiayue Wang, Bilge Yildiz, and William J. Bowman, Nanoscale **14** (3), 663 (2022).
[53] Daniel Mutter, Cong Tao, Daniel F. Urban, and Christian Elsässer, Advanced Engineering Materials **25** (18), 2201847 (2023).
[54] Huiming Guo, Christopher Mead, Marquez Balingit, Soham Shah, Xin Wang, Mingjie Xu, Ich Tran, Toshihiro Aoki, Jack D. Samaniego, Kandis Leslie Gilliard-AbdulAziz, Lincoln J. Lauhon, and William J. Bowman, Matter (2024).
[55] Jiayue Wang, Komal Syed, Shuai Ning, Iradwikanari Waluyo, Adrian Hunt, Ethan J. Crumlin, Alexander K. Opitz, Caroline A. Ross, William J. Bowman, and Bilge Yildiz, Advanced Functional Materials **32** (9), 2108005 (2022).
[56] Nick A. Shepelin, Zahra P. Tehrani, Natacha Ohannessian, Christof W. Schneider, Daniele Pergolesi, and Thomas Lippert, Chemical Society Reviews **52** (7), 2294 (2023).

[57] Huiming Guo, Xin Wang, Alexander D. Dupuy, Julie M. Schoenung, and William J. Bowman, Journal of Materials Research **37** (1), 124 (2022).
[58] Renjie Xie, Xiangchen Hu, Yanuo Shi, Zhiwei Nie, Nian Zhang, Enrico Traversa, Yi Yu, and Nan Yang, ACS Applied Energy Materials **3** (8), 7988 (2020).
[59] J. L. MacManus-Driscoll, Matthew P. Wells, Chao Yun, Jung-Woo Lee, Chang-Beom Eom, and Darrell G. Schlom, APL Materials **8** (4), 040904 (2020).
[60] Hyeon Han, Jucheol Park, Sang Yeol Nam, Kun Joong Kim, Gyeong Man Choi, Stuart S. P. Parkin, Hyun Myung Jang, and John T. S. Irvine, Nature Communications **10** (1), 1471 (2019).
[61] Jiayue Wang, Jing Yang, Alexander K. Opitz, William Bowman, Roland Bliem, Georgios Dimitrakopoulos, Andreas Nenning, Iradwikanari Waluyo, Adrian Hunt, Jean-Jacques Gallet, and Bilge Yildiz, Chemistry of Materials **33** (13), 5021 (2021).
[62] Jenna L. Wardini, Hasti Vahidi, Huiming Guo, and William J. Bowman, Frontiers in Chemistry **9** (2021).
[63] Jiayue Wang, Abinash Kumar, Jenna L. Wardini, Zhan Zhang, Hua Zhou, Ethan J. Crumlin, Jerzy T. Sadowski, Kevin B. Woller, William J. Bowman, James M. LeBeau, and Bilge Yildiz, Nano Letters **22** (13), 5401 (2022).
[64] George F. Harrington, Lixin Sun, Bilge Yildiz, Kazunari Sasaki, Nicola H. Perry, and Harry L. Tuller, Acta Materialia **166**, 447 (2019).
[65] G. W. Lorimer, Mineralogical Magazine **51** (359), 49 (1987).
[66] G. Cliff and G. W. Lorimer, Journal of Microscopy **103** (2), 203 (1975).
[67] Xiaorui Tong, David S. Mebane, and Roger A. De Souza, Journal of the American Ceramic Society **103** (1), 5 (2020).
[68] Si-Young Choi, Sung-Dae Kim, Minseok Choi, Hak-Sung Lee, Jungho Ryu, Naoya Shibata, Teruyasu Mizoguchi, Eita Tochigi, Takahisa Yamamoto, Suk-Joong L. Kang, and Yuichi Ikuhara, Nano Letters **15** (6), 4129 (2015).
[69] Dawei Pang, Wei Li, Ningqiang Zhang, Hong He, Shengcheng Mao, Yanhui Chen, Liwei Cao, Chong Li, Ang Li, and Xiaodong Han, Journal of Rare Earths (2023).
[70] Neven Biškup, Juan Salafranca, Virat Mehta, Mark P. Oxley, Yuri Suzuki, Stephen J. Pennycook, Sokrates T. Pantelides, and Maria Varela, Physical Review Letters **112** (8), 087202 (2014).
[71] Sangwook Joo, Arim Seong, Ohhun Kwon, Kyeounghak Kim, Jong Hoon Lee, Raymond J. Gorte, John M. Vohs, Jeong Woo Han, and Guntae Kim, Science Advances **6** (35), eabb1573.
[72] Ohhun Kwon, Sivaprakash Sengodan, Kyeounghak Kim, Gihyeon Kim, Hu Young Jeong, Jeeyoung Shin, Young-Wan Ju, Jeong Woo Han, and Guntae Kim, Nature Communications **8** (1), 15967 (2017).
[73] Sieun Chae, Logan Williams, Jihang Lee, John T. Heron, and Emmanouil Kioupakis, npj Computational Materials **8** (1), 95 (2022).
[74] Doruk Aksoy, Huolin L. Xin, Timothy J. Rupert, and William J. Bowman, arXiv (2023).
[75] Jian Han, Spencer L. Thomas, and David J. Srolovitz, Progress in Materials Science **98**, 386 (2018).
[76] S. Turner, H. Idrissi, A. F. Sartori, S. Korneychuck, Y. G. Lu, J. Verbeeck, M. Schreck, and G. Van Tendeloo, Nanoscale **8** (4), 2212 (2016).

[77] Peng Ren, Miao Song, Jaewon Lee, Jian Zheng, Zexi Lu, Mark Engelhard, Xiuchun Yang, Xiaolin Li, David Kisailus, and Dongsheng Li, Advanced Materials Interfaces **6** (17), 1901121 (2019).
[78] Mitsuo Takeda and Jun Suzuki, J. Opt. Soc. Am. A **13** (7), 1495 (1996).
[79] M. J. Hÿtch, E. Snoeck, and R. Kilaas, Ultramicroscopy **74** (3), 131 (1998).
[80] Hongchu Du, *GPA:: Geometric Phase Analysis software*. (2018).
[81] Lixin Sun, Dario Marrocchelli, and Bilge Yildiz, Nature Communications **6** (1), 6294 (2015).
[82] Dario Marrocchelli, Lixin Sun, and Bilge Yildiz, Journal of the American Chemical Society **137** (14), 4735 (2015).